Directed energy deposition of γ/γ' Co-Al-W superalloys

Boryung Yoo[a], Chanwon Jung[a,b], KenHee Ryou[a], Won Seok Choi[a], Lukas Haußmann[c], Sangsun Yang[d], Torben Boll[e,f], Steffen Neumeier[c], Pyuck-Pa Choi[a,*]

a. Department of Materials Science and Engineering, Korea Advanced Institute of Science and Technology, 291 Daehak-ro, Yuseong-gu, Daejeon, 34141, Republic of Korea

b. Max-Planck-Institut für Eisenforschung GmbH, Max-Planck-Straße 1, 40237 Düsseldorf, Germany

c. Department of Materials Science and Engineering, Friedrich-Alexander-Universität Erlangen-Nürnberg (FAU), Institute I, Martensstr. 5, 91058 Erlangen, Germany

d. 3D printing Materials Center, Korea Institute of Materials Science, 797 Changwon-daero, Changwon-si, Gyeongnam, 51508, Republic of Korea

e. Karlsruhe Nano Micro Facility (KNMF), Karlsruhe Institute of Technology, Hermann-von-Helmholtz-Platz 1, 76344 Eggenstein-Leopoldshafen, Germany

f. Institute for Applied Materials (IAM-WK), Karlsruhe Institute of Technology, Hermann-von-Helmholtz-Platz 1, 76344 Eggenstein-Leopoldshafen, Germany

*Corresponding author : p.choi@kaist.ac.kr

Abstract

In this study, Co-Al-W superalloys forming γ/γ' microstructures were fabricated by laser-directed energy deposition and investigated with respect to their susceptibility to hot-cracking during manufacturing. Two alloys of different nominal compositions (Co-12Al-8W, Co-7Al-8W (at.%)) were deposited to characterize their microstructures on multiple length scales. While the as-deposited Co-12Al-8W alloy was free of cracks, the Co-7Al-8W alloy exhibited numerous cracks, particularly along high-angle grain boundaries due to internal oxidation cracking. The former Al-rich alloy showed a continuous and dense-packed Al_2O_3 scale on its

surface, preventing internal oxidation. After homogenization heat-treatment at 1300°C for 24 h and subsequent aging at 900°C for 24 h, the Co-12Al-8W alloy revealed a homogeneous γ/γ' microstructure without hot-cracking. By contrast, the Co-7Al-8W alloy did not exhibit a passivation layer but only internal Al_2O_3 particles due to the reduced Al content and insufficiently fast transport of Al to the oxidation front. These particles acted as stress concentration and crack initiation sites during directed energy deposition, thereby limiting the printability of the Co-7Al-8W alloy. The compressive creep results reveal a similar creep resistance of crack-free Co-12Al-8W alloy compared to conventionally processed ternary Co-Al-W alloys.

1. Introduction

The discovery of a γ/γ' microstructure similar to that of Ni-based superalloys has attracted a lot of interest in Co-Al-W alloys [1] as promising high-temperature alloys for gas turbine applications [2–4]. Since Co has a higher melting temperature than Ni [5] and γ/γ' Co-based superalloys exhibit positive lattice misfits [6], Co-based systems show potential for enhanced high-temperature stability and creep resistance as compared to their Ni-based counterparts [6].

Until now, Co-Al-W-based alloys have been mostly fabricated by traditional casting methods [7,8]. However, due to the complexity of the gas turbine components, such as turbine blades including cooling channel arrays, additive manufacturing (AM) of Co-Al-W alloys is of great technological interest. AM enables the fabrication of complex three-

dimensional parts of net-shape and has undergone rapid developments in recent years [9–11]. In addition, directed energy deposition (DED) [12,13] is a specific type of AM based on directing energy from a source on a feedstock material, such as a powder, and fusing and solidifying the material layer-by-layer on a substrate. Another reason Co-based superalloys are attracting attention as suitable materials for AM is their excellent weldability [14–18]. The AM is amenable to weldable alloys [19] and the weldability of conventional Co-based superalloys is known as superior and enough to use as wear-resistant coating [17]. There are several reasons why Co-Al-W alloys exhibit excellent weldability. First, Co-Al-W-based superalloys have a low γ' solvus temperature and high solidus temperature and liquidus temperature, i.e. good hot workability [1,15]. Moreover, the γ' precipitates of Co-based superalloys are known to show a lower deformation resistance compared to those of Ni-based superalloys, which could decrease the strain age cracking susceptibility [20,21]. Furthermore, Co-based superalloys usually show a low degree of segregation during solidification than Ni-based superalloys leading to the reduction of heat affected zone cracking susceptibility [22–24].

The feasibility of AM was demonstrated for several Ni-based superalloys [25–28]. However, a serious issue of AM of superalloys is the formation of hot-cracks during manufacturing, in particular for alloys that contain more than 6 wt.% of the γ' forming elements Al and Ti [29]. Hariharan et al. [30] studied the effects of solute enrichments and grain boundary misorientation on solidification cracking in Inconel 738LC manufactured by selective laser melting (SLM). Chen et al. [31] investigated liquation cracking in the Inconel 718 fabricated by SLM for varying heat input, scanning speed, and grain boundary misorientation. Zhang et al. [32] observed ductility-dip cracking at triple junctions of grain boundaries and the tip of

3

liquation cracks in the Inconel 738 fabricated by DED. According to the above studies, it is generally accepted to be difficult to print the superalloys containing more than 6wt.% of Al and Ti, which induces severe hot-cracking during AM regardless of processing parameters.

AM of a few Co-based alloys such as Co-Cr-Mo [33–39], Co-Ni-based alloy [24,40,41], and Co-based superalloys [42–45] was reported as well. Aydogan et al. [42] investigated the fabricability of commercial T800 alloy with different mixture compositions of NiCr alloys by laser DED. Wei et al. [43] showed that the as-SLM built GH5188 Co-based superalloy exhibits excellent mechanical properties including nano-hardness, tensile strength, and ductility compared to forging and casting samples. Park et al. [44,45] manufactured Co-Ni-W-Al alloys with γ/γ' microstructures using ink-extrusion three-dimensional printing and pack-cementation surface alloying. In addition, Athira et al. [18] and Haußmann et al. [15] recently reported that Co-based superalloys were free of post-weld heat treatment (PWHT) cracking or strain age cracking using laser welding similar to AM. However, to the best of the authors' knowledge, no reports exist on additively manufactured Co-Al-W alloys, which form the fundamental basis for the design of novel γ/γ'-strengthened Co-based superalloys. In this work, we fabricated two alloys of Co-12Al-8W and Co-7Al-8W (at.%) by DED and investigated their microstructure. We could reveal substantial differences in the hot-cracking behavior and the formation of an external or internal Al_2O_3 phase, depending on the amount of Al. Then compressive creep experiments were performed on the crack-free alloy to evaluate its creep resistance at high-temperature.

2. Material and methods

2.1 Sample preparations

Two master alloys were fabricated by vacuum induction melting and gas-atomized to powders. The powders were sieved to obtain particles of 45 ~ 150 μm in size. The particle size distribution and oxygen contents of powders after sieving are shown in Fig. S1 and Table S2 in supplementary materials. A DED machine (InssTek MX-3) equipped with an ytterbium fiber laser of 1,070 nm wavelength was used to fabricate samples of $3\times20\times30$ mm^3 in dimension on carbon steel (S45C) substrate. A laser power of 400 W, a scan speed of 0.85 m/min, a hatch spacing of 0.5 mm, a laser dwell time of 3.5 seconds and a powder feed rate of 4 g/min were used as deposition parameters, using 7 L/min of Ar as a powder carrier and shielding gas. As-deposited Co-12Al-8W specimens were homogenized at 1300°C for 24 h and subsequently aged at 900°C for 24 h, similar to heat-treatments for conventional cast alloys [46], to remove the residual stress and obtain γ/γ' microstructures. The differential scanning calorimeter (DSC) was employed to determine the heat treatment condition (Fig. S3).

To investigate the creep behavior, the crack-free Co-12Al-8W samples were fabricated of $14\times14\times12$ mm^3 in dimension with deposition parameters described above (see Fig. S4). After identical heat-treatments, cylindrical specimens with a diameter of 5 mm and a length of 7.5 mm were produced by electro discharge machining. To avoid the effect of surface roughness and surface oxide or diffusion from the substrate, the compressive creep specimens were machined from the interior of bulk specimen (Fig. S4(e)). No cracks or oxides were observed in the specimens processed for the creep test (Fig. S4(f) and (g)). Creep experiments were conducted using a custom-built pneumatic compression creep testing machine at temperatures

of 800, 850, and 900°C and stresses of 300, 350, and 400 MPa.

2.2 Characterization methods

The compositions of the powders and as-deposited specimens, determined by inductively coupled plasma optical emission spectroscopy (ICP-OES), are listed in Table 1. Microstructural characterization was done by scanning electron microscopy (SEM) (Hitachi SU5000, SU8230) in backscattered electron (BSE) imaging mode, energy dispersive X-ray spectroscopy (EDS), and electron backscatter diffraction (EBSD) (Bruker QUANTAX CrystAlign 400). X-ray diffraction (XRD) (RIGAKU SmartLab, Cu Kα radiation) analyses were conducted in the θ-2θ mode. To analyze the surface oxides, grazing incidence X-ray diffraction (GIXRD) (RIGAKU D/MAX-2500) was performed at an incidence angle of 2°. X-ray microscopy (XRM) (ZEISS Xradia 520 Versa) was performed at an acceleration voltage of 160 kV to image the three-dimensional path and morphology of the cracks. Focused ion beam milling (FEI Helios G4, ZEISS Auriga) was applied for the preparation of transmission electron microscope (TEM) and atom probe tomography (APT) specimens. TEM investigations were conducted (FEI Talos F200X operated at 200kV) in combination with scanning TEM (STEM) – EDS analyses. APT (CAMECA LEAP 4000X HR) analyses were conducted in pulsed UV-laser mode at a base temperature of 50 K, a laser pulse frequency of 100 kHz, a pulse energy of 100 pJ, and a detection rate of 0.5%.

Table 1 Compositions of powder and as-deposited specimens determined by ICP-OES

Alloy	Sample Condition	Co (at.%)	Al (at.%)	W (at.%)
Co-12Al-8W	Powder	bal.	12.1	7.6
	As-deposited	bal.	12.0	7.6

Co-7Al-8W	Powder	bal.	7.2	7.9
	As-deposited	bal.	6.7	9.5

3. Results and discussion

3.1 Cracking behavior of DED-fabricated Co-Al-W alloys

Fig. 1(a) and (b) show the Co-12Al-8W and Co-7Al-8W alloy powders, respectively. The powder particles were nearly spherical in shape and showed a face-centered cubic (FCC) crystal structure (Fig. S5). A schematic figure of the DED process, the applied laser scan strategy, and the specimen dimensions are shown in Fig. 1(c). Fig. 1(d) and (e) reveal striking differences in the surface morphology of the as-deposited alloys. While the surface of the Co-12Al-8W alloy was smooth and did not exhibit any macroscopic defects, the surface of the Co-7Al-8W alloy was rough and revealed several cracks indicated by white arrows. Although some samples showed release from the substrate after the DED process as shown in Fig. 1(d), no cracks were observed in the Co-12Al-8W alloy. From this, it can be expected that the separation between the sample and the substrate occurred not because of the high thermal stress but due to the poor surface of the substrate or lack of fusion. Most specimens investigated in this study adhered well to the substrate (see Fig. S4 and S6). Moreover, differences in crack formation between these two alloys could be clearly observed using XRM. XRM tomogram of the Co-12Al-8W alloy did not reveal any micro-cracks (Fig. 1(f)). In contrast, XRM analysis of the Co-7Al-8W alloy displayed a high density of micro-cracks and voids, where the crack widths and void sizes amounted to ~ 100 μm (Fig. 1(g)). Thus, the Al content was critical for the crack susceptibility and the printability of Co-Al-W alloys.
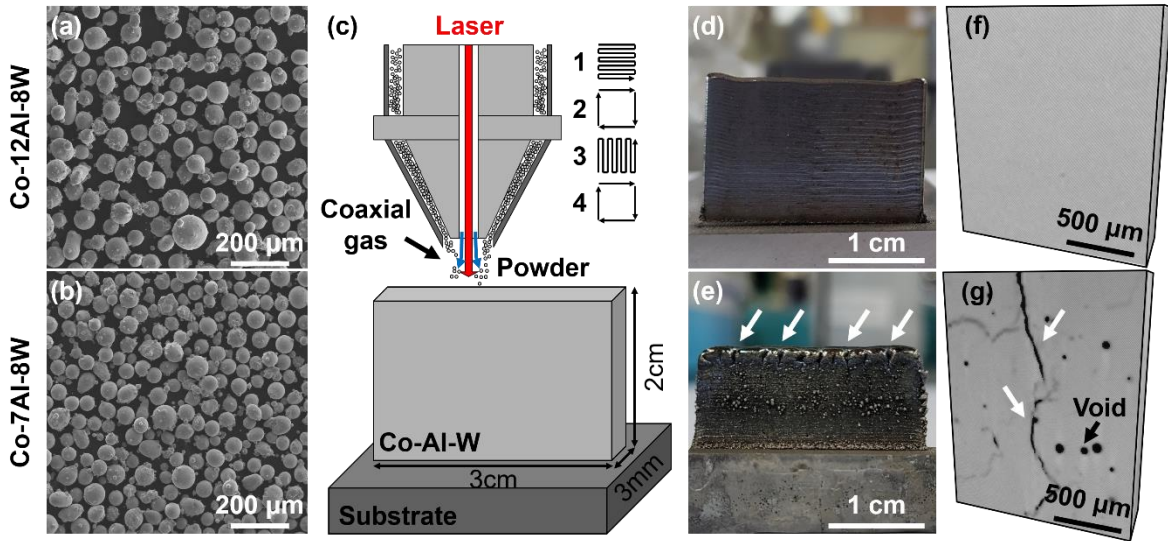
Figure 1 Powder feedstock used for DED: (a) Co-12Al-8W and (b) Co-7Al-8W alloy; (c) schematic figure of the DED process, including the track of the laser beam; surface morphology of (d) Co-12Al-8W and (e) Co-7Al-8W; XRM tomograms of the (f) Co-12Al-8W and (g) Co-7Al-8W alloy taken from the middle of specimens. White arrows indicate the cracks.

Cross-sectional SEM-EDS maps of the two alloys are shown in Fig. 2. A continuous Al_2O_3 oxide layer of ~ 4 μm in thickness was detected on the surface of the Co-12Al-8W alloy (Fig. 2(a)-(c)). Below the Al_2O_3 layer, a heterogeneous distribution of complex oxides comprising Co, Al, and W was detected. The low magnification SEM images of as-deposited Co-12Al-8W alloy that show the surface Al_2O_3 layer and absence of Al_2O_3 particles and cracks within the alloy are shown in Fig. S7. However, the Co-7Al-8W alloy revealed a crack and an external discontinuous surface oxide of ~ 1 μm in thickness, which was identified as Co_3O_4 (Fig. 2(f)). Several Al_2O_3 islands (Fig. 2(e)), which could not be detected by GIXRD presumably due to their low volume fraction, were formed in between Co_3O_4 regions.
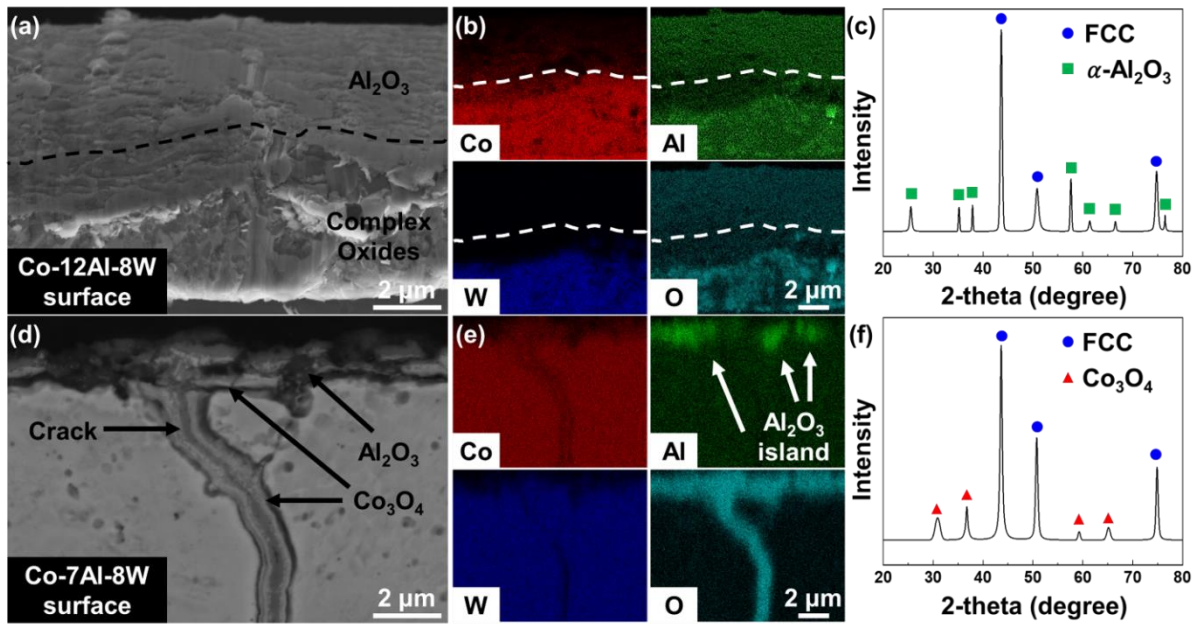
Figure 2 As-deposited Co-12Al-8W alloy of (a) SEM image of cross-sectional surface; (b) EDS maps of the region in (a); (c) corresponding GIXRD pattern; As-deposited Co-7Al-8W alloy of (d) SEM image of cross-sectional surface; (e) EDS maps of the region in (d); (f) corresponding GIXRD pattern.

Fig. 3 shows correlative SEM-EDS, XRM, and EBSD maps of an identical region in the Co-7Al-8W alloy, exhibiting cracks, voids, and oxide particles. Regions highlighted with a cyan color in Fig. 3(b) represent oxides inside the bulk alloy. Fig. 3(d) reveals two Al-oxide particles of ~ 10 μm in size, formed at a high-angle grain boundary (HAGB) (see Fig. 3(c)). These two particles were connected by a thin Al_2O_3 film decorating the same HAGB, however, without any cracks nearby. Uncracked Al-oxide observed by TEM is also shown in Fig. S8. These internal Al_2O_3 particles were probably formed by oxygen diffusing through the external Co_3O_4 layer into the metal along the HAGB and reacting with Al. Some of the internal Al_2O_3 particles acted as crack initiation sites (Fig. 3(e)). As the Al_2O_3 particle broke apart, a crack nucleated and crossed the entire particle. Besides the pronounced cracking

9

along Al_2O_3 particles at HAGBs, grain interior cracking, which appeared to be a branch of a neighboring macro-crack was also observed (Fig. 3(c)). The detailed mechanisms of internal oxidation and cracking will be explained in the following section 3.2.
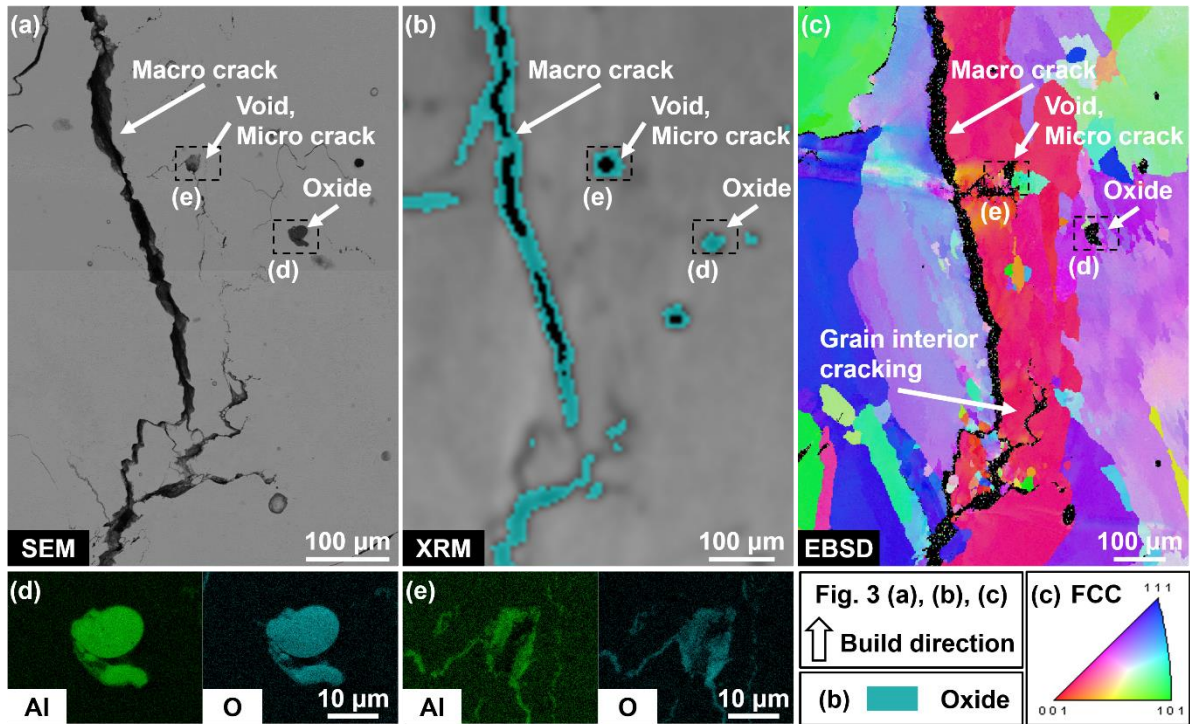

Figure 3 Correlative SEM-EDS, XRM, and EBSD maps of the as-deposited Co-7Al-8W alloy, revealing cracks, voids, and oxides. (a) Cross-sectional SEM image; (b) 2D slice through XRM tomogram; (c) EBSD inverse pole figure (IPF) map. (b) and (c) show the same region of interest as shown in (a); EDS maps of (d) oxide and (e) cracked oxide.

3.2 Hot-cracking mechanism

We detected external Al_2O_3 for both Co-12Al-8W and Co-7Al-8W alloys, however, only the former showed a thick and continuous Al_2O_3 scale (Fig. 2). Although Ar was used as a shielding gas during the manufacturing, Al_2O_3 formed due to oxygen in the DED chamber (As mentioned in the supplementary materials Table S2, the oxygen contents of the powders were very low). Al_2O_3 shows the lowest standard Gibbs free energy of formation among all Co-, Al-, and W-oxides [47]. Due to a reduced Al content, the Co-7Al-8W alloy did not form a continuous Al_2O_3 scale. The observations in this work are in agreement with Ref. [48], which thermodynamically assessed the stability of oxide phases in Co-8.1Al-8.4W and Co-10Al-8W alloys.

The external Al_2O_3 scale formation is dependent on the Al concentration [49], where the critical Al composition for forming external Al_2O_3 is inversely proportional to $D_{Al}^{1/2}$, the square root of the Al diffusivity [50]. It was reported that the interdiffusion coefficient of Al in FCC-Co increases with Al concentration at elevated temperatures [51,52]. As a result, the increase in Al concentration from 7 (Co-7Al-8W) to 12 at.% (Co-12Al-8W) promotes the formation of external Al_2O_3 not only by an enhanced thermodynamic driving force but also by an enhanced Al diffusivity. According to recent oxidation studies on Co-based superalloys [53,54], more than 11 at.% of Al is required to induce the formation of an external Al_2O_3 layer, which is in agreement with the observations of this work.

The continuous and dense Al_2O_3 surface layer of Co-12Al-8W alloy acted as a diffusion barrier, substantially lowering the oxygen transport to the bulk alloy [44,55]. Therefore, internal oxidation and, most importantly, the cracking were suppressed. Since the difference between solidus and liquidus temperature, freezing range, was only about 10°C (Fig. S3), this

alloy did not exhibit liquation or solidification cracks, as common for Ni-based superalloys [56–58]. As a result, the Co-12Al-8W alloy showed superior printability under laser-DED fabrication.

In contrast, the Co-7Al-8W alloy formed Al_2O_3 islands embedded in a discontinuous Co_3O_4 layer on its surface. Co_3O_4 is a non-compact and non-protective oxide [59], which can be easily penetrated by oxygen [60]. Oxygen atoms indeed diffused along the grain boundaries of the Co-7Al-8W alloy to form internal Al_2O_3 particles since the grain boundary diffusivity of oxygen within metals is 10^4 to 10^6 times higher than its lattice diffusivity [61]. In particular, it was reported that random HAGBs can act as fast channels for oxygen diffusion [62–64].

Thermal gradients induced by cyclic heating and cooling during DED can lead to severe thermal stresses and tensile stresses can act on vertically aligned columnar grain boundaries due to material shrinkage during the solidification and cooling process [65]. Thermal stresses acting on thin-walled DED specimens are estimated to be on the order of several hundred MPa [66–68]. In addition, internal Al_2O_3 particles can act as stress concentration sites due to a difference in coefficients of thermal expansion (CTE) as compared to the alloy matrix. The CTE of Al_2O_3 and Co-9Al-9W are reported to be ~ 8×10^{-6}/°C [69] and ~ 1.2 - 1.6×10^{-5}/°C [70], respectively, below 1000°C. Thus, the matrix expands more than the Al_2O_3 particles during heating and induces tensile stress on the particles. Moreover, in the previous studies [71,72] which assess the CTE effect between alumina inclusion and RR1000 Ni-based superalloys, upon cooling from the heat treatment steps, the RR1000 matrix was contracting more than the alumina inclusion, thereby forcing the matrix adjacent to the inclusion into a compressive stress state. These stresses are expected to be substantially higher than the critical stress of ~ 270 MPa, above which micro-cracking in Al_2O_3 is induced according to

Ref [73,74]. Since brittle Al_2O_3 particles cannot accommodate plastic deformation, they are preferential void and crack nucleation sites. Al_2O_3 particles form long films along random HAGBs in the Co-7Al-8W alloy, giving rise to even macro-cracks.

Recently, the crack-free and creep resistant AD730 Ni-based superalloys were achieved with the Boron addition by laser powder bed fusion [75]. In addition, considering that the Boron could alleviate the poor grain boundary cohesivity while inhibiting the internal oxidation [76], similar grain boundary strengthening effect with reduced cracking density also can be expected in the additive manufacturing of Co-Al-W alloys.

3.3   Crack-free microstructure of Co-12Al-8W alloy

A cross-sectional EBSD-IPF map of the as-deposited Co-12Al-8W specimen is shown in Fig. 4(a). Columnar grains were formed approximately along the build direction due to a steep temperature gradient toward the substrate [77]. The columnar grains were tilted with respect to the build direction in a zigzag pattern, which could be ascribed to the laser scan path. As-deposited specimens were single-phase FCC (Fig. S5(b)) without γ' precipitates (also observed by TEM and APT analysis, Fig. S9), presumably due to the high cooling rates of thin-wall samples fabricated by laser deposition [32], which range from ~ 100 to 1000°C/s [78]. Fig. 4(b) shows that the initially columnar grains of the Co-12Al-8W alloy transformed into equiaxed grains of several hundreds of micrometers after homogenization and aging. Recrystallization is the sign of dislocation stored during the DED process due to high thermal stresses causing local plastic deformation [79]. These grains exhibited cuboidal γ' precipitates regularly aligned within the γ matrix (Fig. 4(b) and (d)). In addition, no other phase besides γ and γ' was detected by XRD in the aged Co-12Al-8W alloy (Fig. 4(c)). The γ/γ′ lattice misfit was obtained by the equation of $\delta=2(a_{\gamma'}-a_\gamma)/(a_{\gamma'}+a_\gamma)$, where $a_{\gamma'}$ and a_γ are the lattice parameters

of the γ' and γ phases, respectively [80]. The measured room temperature γ/γ′ lattice misfit was ~ 0.3% ($a_{γ′}$ = 3.60 Å, $a_γ$ = 3.59 Å) by fitting the (111) peaks of FCC and L1$_2$ using Pseudo-Voigt functions, as shown in the inset of Fig. 4(c). Furthermore, the APT measurement (Fig. 4(d)) revealed that Co partitioned to γ while Al and W partitioned to the γ' phase, as reported for cast Co-Al-W alloys [81]. The γ' volume fraction calculated using the lever rule [81] was ~ 64% and thus within the range of values yielding optimal creep resistance for single crystal Ni-based superalloys [82].
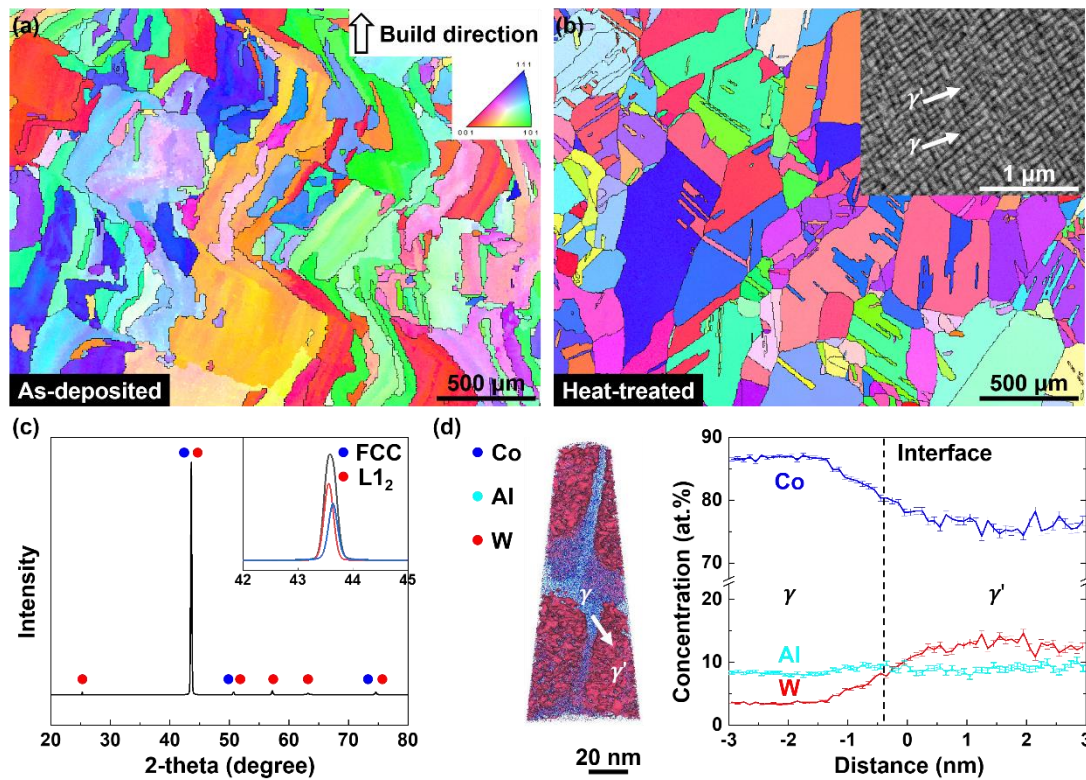

Figure 4 EBSD inverse pole figure (IPF) map of (a) as-deposited and (b) homogenized and aged Co-12Al-8W alloy. The inset shows a magnified BSE image of the γ/γ' microstructure formed after heat-treatment; (c) XRD scan of the heat-treated specimen. The inset shows a detailed scan in the 2θ range from 42° to 45°; (d) a three-dimensional atom map and corresponding proximity histogram of the heat-treated specimen.

14

3.4 Compressive creep of Co-12Al-8W alloy

The compressive creep properties of aged Co-12Al-8W alloys were summarized in Fig. 5 at three different temperatures and stresses. Fig. 5(a) and (b) showed the typical compressive creep curves of Co-Al-W superalloys [83]. Fig. 5(a) revealed that the strain rate decreased as the stress decreased at 850°C. As expected, when the stress was fixed at 400 MPa (Fig. 5(b)), the strain rate decreased as the temperature decreased and the shapes of the creep curves were similar at different temperatures and stresses.

The compressive creep behavior is known to follow a creep power-law equation [84]:

$$\dot{\varepsilon} = A\sigma^n \exp(-Q/RT)$$

where $\dot{\varepsilon}$ is the creep strain rate in the secondary creep regime (here, the minimum strain rate), A is a constant, n is the stress exponent, σ is the applied stress, Q is the creep activation energy, R is the ideal gas constant, and T is the absolute temperature. The stress exponent of DED specimen, which describes the stress-dependence of the alloy under creep conditions, is plotted in Fig. 5(c) with reference of the minimum strain rate of polycrystalline Co-Al-W-(B) alloys and single crystal alloy at 850°C [85]. The calculated stress exponent of Co-12Al-8W alloy was about 11. This is similar to the stress exponents of cast, polycrystalline Co-Al-W-based superalloys, since they exhibit stress exponents of 10 ~ 15 at 850°C [86]. Furthermore, the minimum strain rates of the studied alloys are somewhat higher than the B-containing alloys and single crystal alloy, probably due to the insufficient grain boundary strength of the DED specimens. Interestingly, DED-fabricated Co-12Al-8W shows a much lower minimum strain rate than the conventional cast B-free Co-9Al-9W alloy plotted as a black dot. However, as the Al and W content differ between the two alloys, further investigations on conventional

15

cast Co-12Al-8W with the same grain size would have to be performed for a direct comparison. This shows the potential of the high-temperature application of the DED-fabricated alloys developed in this study. Considering the grain boundary strengthening effect of B on the cast alloys (Fig. 5(c)), the minimum strain rate of Co-12Al-8W alloy could be strongly decreased by several orders as well with B addition.

The creep activation energy is also calculated using creep power-law equation (Fig. 5(d)). Co-12Al-8W alloys showed about 456 kJ/mol, which is in between the lattice diffusion of Co (280 kJ/mol) [87] and the activation energy of Co-9Al-9W-0.12B (742 kJ/mol) [88]. Further study will be performed to elucidate the creep mechanism of DED specimens including deformation mechanisms, diffusion, and microstructural evolution.
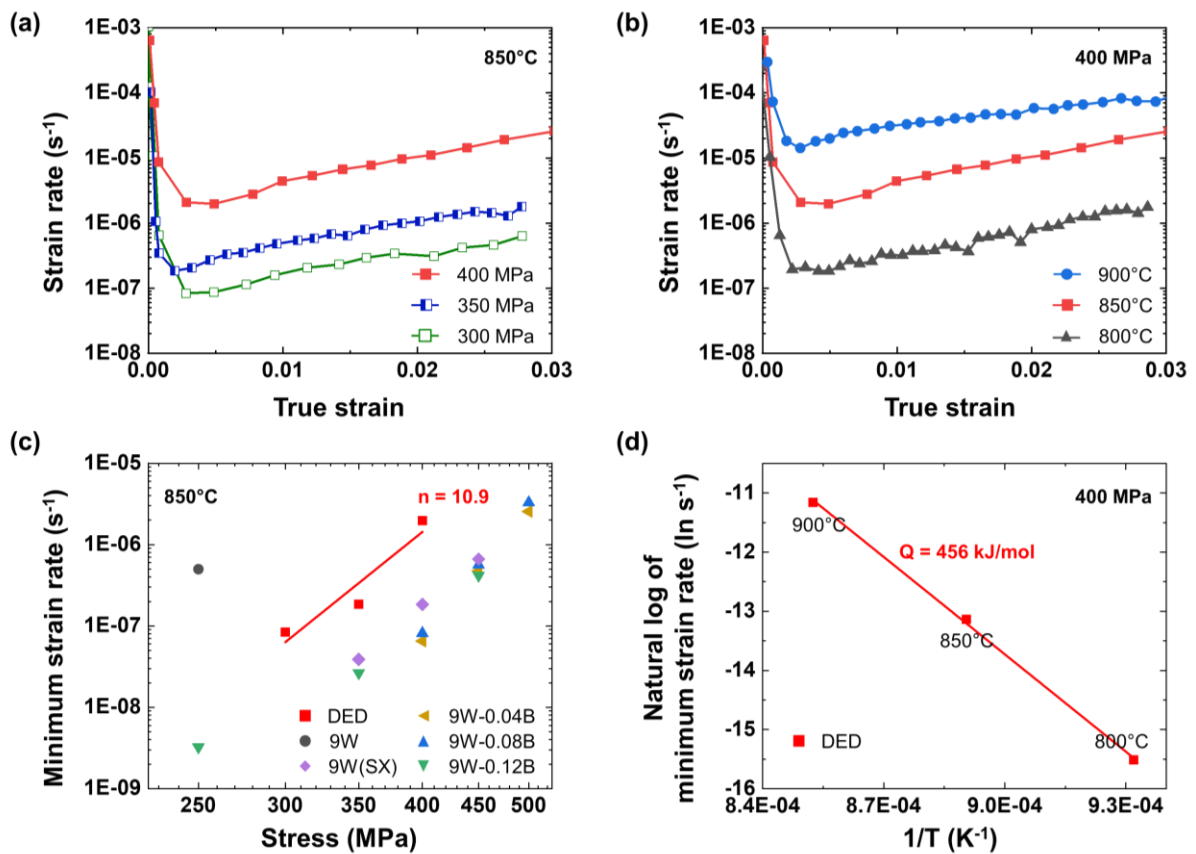
Figure 5 Creep curves of Co-12Al-8W alloy manufactured by DED and several reference alloys. (a) creep strain and strain rate of DED specimen performed at 850°C with several stresses; (b) creep strain and strain rate of DED specimen performed at 400 MPa with several temperatures; (c) applied stress and minimum strain rate of Co-12Al-8W manufactured by DED and reference cast alloys [85] tested at 850°C. (d) reciprocal absolute temperature and the natural log of minimum strain rate performed at 400 MPa. The red slopes in (c) and (d) provide the stress exponent and the activation energy of the DED specimens.

4. Conclusions

In summary, we compared the crack susceptibility of two Co-Al-W alloys during DED. We demonstrated that crack-free fabrication of the Co-12Al-8W alloy is feasible, as it forms a protective external Al_2O_3 scale. We conclude that the printability of Co-Al-W alloys fabricated under laser-DED processing conditions strongly depends on the Al content and in particular on whether an external or internal Al_2O_3 phase is formed. The Co-12Al-8W alloy forms a crack-free and regular γ/γ' microstructure under standard heat-treatments. Compressive creep properties of printed Co-12Al-8W alloy show better creep strength compared to a B-free Co-9Al-9W alloy manufactured by casting.

References

[1]   J. Sato, T. Omori, K. Oikawa, I. Ohnuma, R. Kainuma, K. Ishida, Cobalt-base high-temperature alloys, Science (80-.). 312 (2006) 90–91. doi:10.1126/science.1121738.

[2]   Y.F. Cui, X. Zhang, G.L. Xu, W.J. Zhu, H.S. Liu, Z.P. Jin, Thermodynamic assessment of Co–Al–W system and solidification of Co-enriched ternary alloys, J. Mater. Sci. 46 (2011) 2611–2621. doi:10.1007/s10853-010-5115-y.

[3]   A. Bauer, S. Neumeier, F. Pyczak, M. Göken, Microstructure and creep strength of different γ/γ′- strengthened Co-base superalloy variants, Scr. Mater. 63 (2010) 1197–1200. doi:10.1016/j.scriptamat.2010.08.036.

[4]   M. Ooshima, K. Tanaka, N.L. Okamoto, K. Kishida, H. Inui, Effects of quaternary alloying elements on the γ′ solvus temperature of Co-Al-W based alloys with fcc/L12 two-phase microstructures, J. Alloys Compd. 508 (2010) 71–78. doi:10.1016/j.jallcom.2010.08.050.

[5]   R.C. Reed, The Superalloys, Cambridge University Press, Cambridge, 2006. doi:10.1017/CBO9780511541285.

[6]   H. Mughrabi, The importance of sign and magnitude of γ/γ′ lattice misfit in superalloys—with special reference to the new γ′-hardened cobalt-base superalloys, Acta Mater. 81 (2014) 21–29. doi:10.1016/j.actamat.2014.08.005.

[7]   I. Lopez-Galilea, C. Zenk, S. Neumeier, S. Huth, W. Theisen, M. Göken, The Thermal Stability of Intermetallic Compounds in an As-Cast SX Co-Base Superalloy, Adv. Eng. Mater. 17 (2015) 741–747. doi:10.1002/adem.201400249.

[8]   S.K. Makineni, B. Nithin, K. Chattopadhyay, Synthesis of a new tungsten-free γ-γ′ Cobalt-based superalloy by tuning alloying additions, Acta Mater. 85 (2015) 85–94. doi:10.1016/j.actamat.2014.11.016.

[9]   T. Keller, G. Lindwall, S. Ghosh, L. Ma, B.M. Lane, F. Zhang, U.R. Kattner, E.A. Lass, J.C. Heigel, Y. Idell, M.E. Williams, A.J. Allen, J.E. Guyer, L.E. Levine, Application of finite element, phase-field, and CALPHAD-based methods to additive manufacturing of Ni-based superalloys, Acta Mater. 139 (2017) 244–253. doi:10.1016/j.actamat.2017.05.003.

[10]   Y.L. Kuo, S. Horikawa, K. Kakehi, Effects of build direction and heat treatment on creep properties of Ni-base superalloy built up by additive manufacturing, Scr. Mater. 129 (2017) 74–78. doi:10.1016/j.scriptamat.2016.10.035.

[11]   S.S. Babu, N. Raghavan, J. Raplee, S.J. Foster, C. Frederick, M. Haines, R. Dinwiddie, M.K. Kirka, A. Plotkowski, Y. Lee, R.R. Dehoff, Additive Manufacturing of Nickel Superalloys: Opportunities for Innovation and Challenges Related to Qualification, Metall. Mater. Trans. A. 49 (2018) 3764–3780. doi:10.1007/s11661-018-4702-4.

[12]   ASTM International, Standard Guide for Directed Energy Deposition of Metals, ASTM Stand. (2016) 1–22. doi:10.1520/F3187.

[13]   ASTM, Guide for Additive Manufacturing — Design — Directed Energy Deposition, Int. Stand. F3413-2019 (2019) 1–24. doi:10.1520/F3413-19.design.

[14]   D. Matthew J, Donachie. Stephen J, Superalloys: A Technical Guide, 2nd Edition, 2002. https://books.google.co.kr/books/about?id=vjCJ5pI1QpkC&redir_esc=y.

[15]   L. Haußmann, B. Burbaum, B. Stöhr, A. Förner, L. Freund, M. Göken, S. Neumeier, Crack-Free Welding of a Co-Base Superalloy with High γ' Precipitate Fraction, Adv. Eng. Mater. 2200609 (2022). doi:10.1002/adem.202200609.

[16]   D. Svetlizky, B. Zheng, A. Vyatskikh, M. Das, S. Bose, A. Bandyopadhyay, J.M. Schoenung, E.J. Lavernia, N. Eliaz, Laser-based directed energy deposition (DED-LB) of advanced materials, Mater. Sci. Eng. A. 840 (2022) 142967. doi:10.1016/j.msea.2022.142967.

[17]   C. Liu, Y. Sun, M. Wen, T. He, J. Yu, Effect of Cr addition on microstructure and welding solidification cracking susceptibility of Co-Al-W based superalloys, J. Manuf. Process. 56 (2020) 820–829. doi:10.1016/j.jmapro.2020.03.049.

[18] K.S. Athira, P. Pandey, K.V.P. Prabhakar, K. Chattopadhyay, S. Chatterjee, Laser welding of a W-free precipitation strengthened Co-base superalloy, J. Mater. Sci. 57 (2022) 7085–7100. doi:10.1007/s10853-022-07117-8.

[19] J.H. Martin, B.D. Yahata, J.M. Hundley, J.A. Mayer, T.A. Schaedler, T.M. Pollock, 3D printing of high-strength aluminium alloys, Nature. 549 (2017) 365–369. doi:10.1038/nature23894.

[20] S. Neumeier, L.P. Freund, M. Göken, Novel wrought γ/γ' cobalt base superalloys with high strength and improved oxidation resistance, Scr. Mater. 109 (2015) 104–107. doi:10.1016/j.scriptamat.2015.07.030.

[21] M.S. Titus, Y.M. Eggeler, A. Suzuki, T.M. Pollock, Creep-induced planar defects in L12-containing Co- and CoNi-base single-crystal superalloys, Acta Mater. 82 (2015) 530–539. doi:10.1016/j.actamat.2014.08.033.

[22] T.M. Pollock, J. Dibbern, M. Tsunekane, J. Zhu, A. Suzuki, New Co-based γ-γ' high-temperature alloys, JOM. 62 (2010) 58–63. doi:10.1007/s11837-010-0013-y.

[23] E.A. Lass, Application of Computational Thermodynamics to the Design of a Co-Ni-Based γ'-Strengthened Superalloy, Metall. Mater. Trans. A Phys. Metall. Mater. Sci. 48 (2017) 2443–2459. doi:10.1007/s11661-017-4040-y.

[24] S.P. Murray, K.M. Pusch, A.T. Polonsky, C.J. Torbet, G.G.E. Seward, N. Zhou, S.A.J. Forsik, P. Nandwana, M.M. Kirka, R.R. Dehoff, W.E. Slye, T.M. Pollock, A defect-resistant Co–Ni superalloy for 3D printing, Nat. Commun. 11 (2020) 1–11. doi:10.1038/s41467-020-18775-0.

[25] C. Pleass, S. Jothi, Influence of powder characteristics and additive manufacturing process parameters on the microstructure and mechanical behaviour of Inconel 625 fabricated by Selective Laser Melting, Addit. Manuf. 24 (2018) 419–431. doi:10.1016/j.addma.2018.09.023.

[26] N. Raghavan, R. Dehoff, S. Pannala, S. Simunovic, M. Kirka, J. Turner, N. Carlson, S.S. Babu, Numerical modeling of heat-transfer and the influence of process parameters on tailoring the grain morphology of IN718 in electron beam additive manufacturing, Acta Mater. 112 (2016) 303–314. doi:10.1016/j.actamat.2016.03.063.

[27] Z. Wang, K. Guan, M. Gao, X. Li, X. Chen, X. Zeng, The microstructure and mechanical properties of deposited-IN718 by selective laser melting, J. Alloys Compd. 513 (2012) 518–523. doi:10.1016/j.jallcom.2011.10.107.

[28] Q. Han, Y. Gu, R. Setchi, F. Lacan, R. Johnston, S.L. Evans, S. Yang, Additive manufacturing of high-strength crack-free Ni-based Hastelloy X superalloy, Addit. Manuf. 30 (2019) 100919. doi:10.1016/j.addma.2019.100919.

[29] J. Xu, X. Lin, P. Guo, H. Dong, X. Wen, Q. Li, L. Xue, W. Huang, The initiation and propagation mechanism of the overlapping zone cracking during laser solid forming of IN-738LC superalloy, J. Alloys Compd. 749 (2018) 859–870. doi:10.1016/j.jallcom.2018.03.366.

[30] A. Hariharan, L. Lu, J. Risse, A. Kostka, B. Gault, E.A. Jägle, D. Raabe,

Misorientation-dependent solute enrichment at interfaces and its contribution to defect formation mechanisms during laser additive manufacturing of superalloys, Phys. Rev. Mater. 3 (2019) 123602. doi:10.1103/PhysRevMaterials.3.123602.

[31]   Y. Chen, K. Zhang, J. Huang, S.R.E. Hosseini, Z. Li, Characterization of heat affected zone liquation cracking in laser additive manufacturing of Inconel 718, Mater. Des. 90 (2016) 586–594. doi:10.1016/j.matdes.2015.10.155.

[32]   X. Zhang, H. Chen, L. Xu, J. Xu, X. Ren, X. Chen, Cracking mechanism and susceptibility of laser melting deposited Inconel 738 superalloy, Mater. Des. 183 (2019) 108105. doi:10.1016/j.matdes.2019.108105.

[33]   X. Zhou, D. Wang, X. Liu, D.D. Zhang, S. Qu, J. Ma, G. London, Z. Shen, W. Liu, 3D-imaging of selective laser melting defects in a Co-Cr-Mo alloy by synchrotron radiation micro-CT, Acta Mater. 98 (2015) 1–16. doi:10.1016/j.actamat.2015.07.014.

[34]   D. Wei, Y. Koizumi, T. Takashima, M. Nagasako, A. Chiba, Fatigue improvement of electron beam melting-fabricated biomedical Co–Cr–Mo alloy by accessible heat treatment, Mater. Res. Lett. 6 (2018) 93–99. doi:10.1080/21663831.2017.1396506.

[35]   D. Wei, A. Anniyaer, Y. Koizumi, K. Aoyagi, M. Nagasako, H. Kato, A. Chiba, On microstructural homogenization and mechanical properties optimization of biomedical Co-Cr-Mo alloy additively manufactured by using electron beam melting, Addit. Manuf. 28 (2019) 215–227. doi:10.1016/j.addma.2019.05.010.

[36]   D. Wei, Y. Koizumi, A. Chiba, K. Ueki, K. Ueda, T. Narushima, Y. Tsutsumi, T. Hanawa, Heterogeneous microstructures and corrosion resistance of biomedical Co-Cr-Mo alloy fabricated by electron beam melting (EBM), Addit. Manuf. 24 (2018) 103–114. doi:10.1016/j.addma.2018.09.006.

[37]   S.H. Sun, Y. Koizumi, S. Kurosu, Y.P. Li, H. Matsumoto, A. Chiba, Build direction dependence of microstructure and high-temperature tensile property of Co-Cr-Mo alloy fabricated by electron beam melting, Acta Mater. 64 (2014) 154–168. doi:10.1016/j.actamat.2013.10.017.

[38]   Z. Wang, S.Y. Tang, S. Scudino, Y.P. Ivanov, R.T. Qu, D. Wang, C. Yang, W.W. Zhang, A.L. Greer, J. Eckert, K.G. Prashanth, Additive manufacturing of a martensitic Co–Cr–Mo alloy: Towards circumventing the strength–ductility trade-off, Addit. Manuf. 37 (2021) 1–14. doi:10.1016/j.addma.2020.101725.

[39]   X.P. Tan, P. Wang, Y. Kok, W.Q. Toh, Z. Sun, S.M.L. Nai, M. Descoins, D. Mangelinck, E. Liu, S.B. Tor, Carbide precipitation characteristics in additive manufacturing of Co-Cr-Mo alloy via selective election beam melting, Scr. Mater. 143 (2018) 117–121. doi:10.1016/j.scriptamat.2017.09.022.

[40]   S.P. Murray, E.B. Raeker, K.M. Pusch, C. Frey, C.J. Torbet, N. Zhou, S.A.J. Forsik, A.D. Dicus, G.A. Colombo, M.M. Kirka, T.M. Pollock, Microstructure Evolution and Tensile Properties of a Selectively Laser Melted CoNi-Base Superalloy, Metall. Mater. Trans. A Phys. Metall. Mater. Sci. 53 (2022) 2943–2960. doi:10.1007/s11661-022-06716-z.

[41]   L. Tang, J. Liang, C. Cui, J. Li, Y. Zhou, X. Sun, Y. Ding, Influence of Co content on

the microstructures and mechanical properties of a Ni–Co base superalloy made by specific additive manufacturing process, Mater. Sci. Eng. A. 786 (2020) 139438. doi:10.1016/j.msea.2020.139438.

[42]   B. Aydogan, H. Sahasrabudhe, Enabling multi-material structures of co-based superalloy using laser directed energy deposition additive manufacturing, Metals (Basel). 11 (2021). doi:10.3390/met11111717.

[43]   W. Wei, J.C. Xiao, C.F. Wang, Q. Cheng, F.J. Guo, Q. He, M.S. Wang, S.Z. Jiang, C.X. Huang, Hierarchical microstructure and enhanced mechanical properties of SLM-fabricated GH5188 Co-superalloy, Mater. Sci. Eng. A. 831 (2022). doi:10.1016/j.msea.2021.142276.

[44]   H. Park, C. Li, A.E. Jakus, R.N. Shah, H. Choe, D.C. Dunand, High-temperature mechanical properties of γ/γ′ Co–Ni–W–Al superalloy microlattices, Scr. Mater. 188 (2020) 146–150. doi:10.1016/j.scriptamat.2020.07.009.

[45]   H. Park, H. Choe, D.C. Dunand, Microstructure and compressive properties of 3D-extrusion-printed, aluminized cobalt-based superalloy microlattices, Mater. Sci. Eng. A. 815 (2021) 141262. doi:10.1016/j.msea.2021.141262.

[46]   H.-Y. Yan, V.A. Vorontsov, D. Dye, Alloying effects in polycrystalline γ′ strengthened Co–Al–W base alloys, Intermetallics. 48 (2014) 44–53. doi:10.1016/j.intermet.2013.10.022.

[47]   I. Barin, Thermochemical Data of Pure Substances, 3rd ed., Wiley, 1995. doi:10.1002/9783527619825.

[48]   L. Klein, A. Zendegani, M. Palumbo, S.G. Fries, S. Virtanen, First approach for thermodynamic modelling of the high temperature oxidation behaviour of ternary γ′-strengthened Co–Al–W superalloys, Corros. Sci. 89 (2014) 1–5. doi:10.1016/j.corsci.2014.08.016.

[49]   C. Wagner, Reaktionstypen bei der Oxydation von Legierungen, Zeitschrift Für Elektrochemie, Berichte Der Bunsengesellschaft Für Phys. Chemie. 63 (1959) 772–782. doi:doi.org/10.1002/bbpc.19590630713.

[50]   C. Wagner, Oxidation of Alloys Involving Noble Metals, J. Electrochem. Soc. 103 (1956) 571–580. doi:10.1149/1.2430159.

[51]   S. Neumeier, H.U. Rehman, J. Neuner, C.H. Zenk, S. Michel, S. Schuwalow, J. Rogal, R. Drautz, M. Göken, Diffusion of solutes in fcc Cobalt investigated by diffusion couples and first principles kinetic Monte Carlo, Acta Mater. 106 (2016) 304–312. doi:10.1016/j.actamat.2016.01.028.

[52]   Y.-W. Cui, B. Tang, R. Kato, R. Kainuma, K. Ishida, Interdiffusion and Atomic Mobility for Face-Centered-Cubic Co-Al Alloys, Metall. Mater. Trans. A. 42 (2011) 2542–2546. doi:10.1007/s11661-011-0758-0.

[53]   C.A. Stewart, A. Suzuki, R.K. Rhein, T.M. Pollock, C.G. Levi, Oxidation Behavior Across Composition Space Relevant to Co-based γ/γ′ Alloys, Metall. Mater. Trans. A. 50 (2019) 5445–5458. doi:10.1007/s11661-019-05413-8.

[54] W. Li, L. Li, S. Antonov, F. Lu, Q. Feng, Effects of Cr and Al/W ratio on the microstructural stability, oxidation property and γ′ phase nano-hardness of multi-component Co–Ni-base superalloys, J. Alloys Compd. 826 (2020) 154182. doi:10.1016/j.jallcom.2020.154182.

[55] H. Choe, D.C. Dunand, Mechanical properties of oxidation-resistant Ni-Cr foams, Mater. Sci. Eng. A. 384 (2004) 184–193. doi:10.1016/j.msea.2004.06.045.

[56] Y. Danis, C. Arvieu, E. Lacoste, T. Larrouy, J.M. Quenisset, An investigation on thermal, metallurgical and mechanical states in weld cracking of Inconel 738LC superalloy, Mater. Des. 31 (2010) 402–416. doi:10.1016/j.matdes.2009.05.041.

[57] J. Zhang, R.F. Singer, Hot tearing of nickel-based superalloys during directional solidification, Acta Mater. 50 (2002) 1869–1879. doi:10.1016/S1359-6454(02)00042-3.

[58] I. Lopez-Galilea, B. Ruttert, J. He, T. Hammerschmidt, R. Drautz, B. Gault, W. Theisen, Additive manufacturing of CMSX-4 Ni-base superalloy by selective laser melting: Influence of processing parameters and heat treatment, Addit. Manuf. 30 (2019) 100874. doi:10.1016/j.addma.2019.100874.

[59] H.Y. Yan, V.A. Vorontsov, D. Dye, Effect of alloying on the oxidation behaviour of Co-Al-W superalloys, Corros. Sci. 83 (2014) 382–395. doi:10.1016/j.corsci.2014.03.002.

[60] A. Motallebzadeh, S.A.A. Dilawary, E. Atar, H. Cimenoglu, High-Temperature Oxidation of Stellite 12 Hardfacings: Effect of Mo on Characteristics of Oxide Scale, J. Mater. Eng. Perform. 28 (2019) 463–474. doi:10.1007/s11665-018-3796-6.

[61] A. Atkinson, Diffusion along grain boundaries and dislocations in oxides, alkali halides and carbides, Solid State Ionics. 12 (1984) 309–320. doi:10.1016/0167-2738(84)90160-7.

[62] U. Krupp, W.M. Kane, X. Liu, O. Dueber, C. Laird, C.J. McMahon, The effect of grain-boundary-engineering-type processing on oxygen-induced cracking of IN718, Mater. Sci. Eng. A. 349 (2003) 213–217. doi:10.1016/S0921-5093(02)00753-0.

[63] Y. Mishin, C. Herzig, Grain boundary diffusion: Recent progress and future research, Mater. Sci. Eng. A. 260 (1999) 55–71. doi:10.1016/s0921-5093(98)00978-2.

[64] S. Yamaura, Y. Igarashi, S. Tsurekawa, T. Watanabe, Structure-dependent intergranular oxidation in Ni-Fe polycrystalline alloy, Acta Mater. 47 (1999) 1163–1174. doi:10.1016/S1359-6454(99)00007-5.

[65] E. Chauvet, P. Kontis, E.A. Jägle, B. Gault, D. Raabe, C. Tassin, J.-J. Blandin, R. Dendievel, B. Vayre, S. Abed, G. Martin, Hot cracking mechanism affecting a non-weldable Ni-based superalloy produced by selective electron Beam Melting, Acta Mater. 142 (2018) 82–94. doi:10.1016/j.actamat.2017.09.047.

[66] T. Mukherjee, W. Zhang, T. DebRoy, An improved prediction of residual stresses and distortion in additive manufacturing, Comput. Mater. Sci. 126 (2017) 360–372. doi:10.1016/j.commatsci.2016.10.003.

[67] Z. Wang, E. Denlinger, P. Michaleris, A.D. Stoica, D. Ma, A.M. Beese, Residual stress mapping in Inconel 625 fabricated through additive manufacturing: Method for neutron diffraction measurements to validate thermomechanical model predictions, Mater. Des. 113 (2017) 169–177. doi:10.1016/j.matdes.2016.10.003.

[68] M. Alimardani, E. Toyserkani, J.P. Huissoon, A 3D dynamic numerical approach for temperature and thermal stress distributions in multilayer laser solid freeform fabrication process, Opt. Lasers Eng. 45 (2007) 1115–1130. doi:10.1016/j.optlaseng.2007.06.010.

[69] D. Dixit, R. Pal, G. Kapoor, M. Stabenau, Lightweight composite materials processing, in: Light. Ballist. Compos., Elsevier, 2016: pp. 157–216. doi:10.1016/B978-0-08-100406-7.00006-4.

[70] K. Tanaka, M. Ooshima, N. Tsuno, A. Sato, H. Inui, Creep deformation of single crystals of new Co-Al-W-based alloys with fcc/L1 2 two-phase microstructures, Philos. Mag. 92 (2012) 4011–4027. doi:10.1080/14786435.2012.700416.

[71] D. Naragani, M.D. Sangid, P.A. Shade, J.C. Schuren, H. Sharma, J.S. Park, P. Kenesei, J. V. Bernier, T.J. Turner, I. Parr, Investigation of fatigue crack initiation from a non-metallic inclusion via high energy x-ray diffraction microscopy, Acta Mater. 137 (2017) 71–84. doi:10.1016/j.actamat.2017.07.027.

[72] R. Bandyopadhyay, M.D. Sangid, Crystal plasticity assessment of inclusion- and matrix-driven competing failure modes in a nickel-base superalloy, Acta Mater. 177 (2019) 20–34. doi:10.1016/j.actamat.2019.07.024.

[73] W. Węglewski, M. Basista, M. Chmielewski, K. Pietrzak, Modeling of thermally induced damage in the processing of Cr–Al2O3 composites, Compos. Part B Eng. 43 (2012) 255–264. doi:10.1016/j.compositesb.2011.07.016.

[74] R.G. Munro, Evaluated material properties for a sintered α-alumina, J. Am. Ceram. Soc. 80 (1997) 1919–1928. doi:10.1111/j.1151-2916.1997.tb03074.x.

[75] A. Després, S. Antonov, C. Mayer, C. Tassin, M. Veron, J.J. Blandin, P. Kontis, G. Martin, On the role of boron, carbon and zirconium on hot cracking and creep resistance of an additively manufactured polycrystalline superalloy, Materialia. 19 (2021). doi:10.1016/j.mtla.2021.101193.

[76] A. Sharma, S. Dixit, N. Baler, P. Agrawal, S.K. Makineni, K. Chattopadhyay, Impact of boron as an alloying addition on the microstructure, thermo-physical properties and creep resistance of a tungsten-free Co-based γ/γ' superalloy, Mater. Sci. Eng. A. 855 (2022) 143899. doi:10.1016/j.msea.2022.143899.

[77] Z. Zhou, L. Huang, Y. Shang, Y. Li, L. Jiang, Q. Lei, Causes analysis on cracks in nickel-based single crystal superalloy fabricated by laser powder deposition additive manufacturing, Mater. Des. 160 (2018) 1238–1249. doi:10.1016/j.matdes.2018.10.042.

[78] S.M. Thompson, L. Bian, N. Shamsaei, A. Yadollahi, An overview of Direct Laser Deposition for additive manufacturing; Part I: Transport phenomena, modeling and diagnostics, Addit. Manuf. 8 (2015) 36–62. doi:10.1016/j.addma.2015.07.001.

[79] P. Kontis, E. Chauvet, Z. Peng, J. He, A.K. da Silva, D. Raabe, C. Tassin, J.J. Blandin, S. Abed, R. Dendievel, B. Gault, G. Martin, Atomic-scale grain boundary engineering to overcome hot-cracking in additively-manufactured superalloys, Acta Mater. 177 (2019) 209–221. doi:10.1016/j.actamat.2019.07.041.

[80] I. Povstugar, C.H. Zenk, R. Li, P.P. Choi, S. Neumeier, O. Dolotko, M. Hoelzel, M. Göken, D. Raabe, Elemental partitioning, lattice misfit and creep behaviour of Cr containing γ′ strengthened Co base superalloys, Mater. Sci. Technol. 32 (2016) 220–225. doi:10.1179/1743284715Y.0000000112.

[81] I. Povstugar, P.P. Choi, S. Neumeier, A. Bauer, C.H. Zenk, M. Göken, D. Raabe, Elemental partitioning and mechanical properties of Ti- and Ta-containing Co-Al-W-base superalloys studied by atom probe tomography and nanoindentation, Acta Mater. 78 (2014) 78–85. doi:10.1016/j.actamat.2014.06.020.

[82] T. Murakumo, T. Kobayashi, Y. Koizumi, H. Harada, Creep behaviour of Ni-base single-crystal superalloys with various γ′ volume fraction, Acta Mater. 52 (2004) 3737–3744. doi:10.1016/j.actamat.2004.04.028.

[83] Y. Li, F. Pyczak, J. Paul, M. Oehring, U. Lorenz, Z. Yao, Microstructure evolution in L12 hardened Co-base superalloys during creep, J. Mater. Res. 32 (2017) 4522–4530. doi:10.1557/jmr.2017.362.

[84] F.R. Long, S.I. Baik, D.W. Chung, F. Xue, E.A. Lass, D.N. Seidman, D.C. Dunand, Microstructure and creep performance of a multicomponent co-based L12–ordered intermetallic alloy, Acta Mater. 196 (2020) 396–408. doi:10.1016/j.actamat.2020.06.050.

[85] A. Bauer, S. Neumeier, F. Pyczak, R.F. Singer, M. Göken, Creep properties of different γ'-strengthened Co-base superalloys, Mater. Sci. Eng. A. 550 (2012) 333–341. doi:10.1016/j.msea.2012.04.083.

[86] A. Bauer, S. Neumeier, F. Pyczak, M. Göken, Creep Strength and Microstructure of Polycrystalline γ′ - Strengthened Cobalt-Base Superalloys, Superalloys 2012. (2012) 695–703. doi:10.1002/9781118516430.ch77.

[87] O.D. Sherby, J. Weertman, Diffusion-controlled dislocation creep: a defense, Acta Metall. 27 (1979) 387–400. doi:10.1016/0001-6160(79)90031-2.

[88] D.J. Sauza, D.C. Dunand, D.N. Seidman, Microstructural evolution and high-temperature strength of a γ(f.c.c.)/γ'(L12) Co–Al–W–Ti–B superalloy, Acta Mater. 174 (2019) 427–438. doi:10.1016/j.actamat.2019.05.058.